Electronic Supplementary Material (ESI) for Energy & Environmental Science.

Supporting Information

Ruthenium nanoparticles decorated with surface hydroxyl and borate species boost the overall seawater splitting via increased hydrophilicity

Le-Wei Shen, Yong Wang, Ling Shen, Jiang-Bo Chen, Yu Liu, Ming-Xia Hu, Wen-Ying Zhao, Kang-Yi Xiong, Si-Ming Wu, Yi Lu, Jie Ying, Maria Magdalena Titirici, Christoph Janiak, Ge Tian*, and Xiao-Yu Yang*

L.-W. Shen, Y. Wang, L. Shen, J.-B. Chen, Y. Liu, M.-X. Hu, W.-Y. Zhao, K.-Y. Xiong, S.-M. Wu, Y. Lu, Prof. G. Tian, and Prof. X.-Y. Yang
State Key Laboratory of Advanced Technology for Materials Synthesis and Processing, and International School of Materials Science and Engineering, and School of Materials Science and Engineering, and Shenzhen Research Institute, and Laoshan Laboratory, Wuhan University of Technology, Wuhan, Hubei, 430070, China
E-mail: xyyang@whut.edu.cn (X.Y.Y.); tiange@whut.edu.cn (G. T.)

Prof. X.-Y. Yang

National Energy Key Laboratory for New Hydrogen-Ammonia Energy Technologies Foshan Xianhu Laboratory, Foshan 528200, P.R.China

J. Ying

School of Chemical Engineering and Technology, Sun Yat-sen University, Zhuhai 519082, China

Prof. M. M. Titirici

Department of Chemical Engineering, Imperial College London, London SW7 2AZ, England, UK

Prof. C. Janiak
Institut für Anorganische Chemie und Strukturchemie, Heinrich-Heine-Universität Düsseldorf, 40204 Düsseldorf, Germany

Experimental Procedures

Chemicals and Materials

All chemicals were analytical grade. Ruthenium (III) chloride hydrate ($RuCl_3 \cdot xH_2O$, 35.0-42.0% Ru basis), ruthenium (IV) oxide (RuO_2), sodium hydroxide (NaOH), sulfuric acid (H_2SO_4), sodium borohydride ($NaBH_4$), hydrazine monohydrate (N_2H_4 H_2O), Nafion (5 wt.%) and isopropyl alcohol (C_3H_8O), potassium thiocyanate (KSCN), were purchased from Shanghai Aladdin Biochemical Polytron Technologies Inc. Commercial Pt/C (20 wt. %) was purchased from Johnson Matthey (Shanghai) Chemicals Co. Ltd. Deionized water (>18 MΩ) was used in all aqueous solutions.

Materials synthesis

Synthesis of Ru-BO_x-OH precursor.

The Ru-BO_x-OH precursor was synthesized by a typical method as follows: 0.5 mL of 0.2 mol L^{-1} $RuCl_3$ was dispersed in 2.5 mL of deionized (DI) water. Then, 1 mL of freshly prepared mixed solution (1.0 mol L^{-1} $NaBH_4$ and 0.1 mol L^{-1} NaOH, pH = 13) was injected into the above solution, then vigorous frothing occurs and the dark precipitate was observed immediately. After 30 minutes, the precipitates were collected by sedimentation and washed with large amount of DI water. After stored the sample in DI water for 24 hours, the final product was obtained by freeze drying.

Synthesis of Ru-BO_x-OH-(200–350).

30 mg of the Ru-BO_x-OH products were subjected to a thermal treatment under high purity argon (Ar) for 2 hours at various temperatures in the range of 200–350 °C, with the heating rate of 5 °C min^{-1}.

Synthesis of Ru-O_x and Ru-O_x-300.

The Ru-O_x was synthesized by a hydrazine hydrate (N_2H_4 H_2O) reduction method[1] and Ru-O_x-300 was produced by thermal treatment: 2 mL of 0.2 mol L^{-1} $RuCl_3$ was dispersed in 8 mL of DI water, then 0.33 mL of NaOH (20 mol L^{-1}) and 1 mL of N_2H_4 H_2O were added into the above solution. After stirring for 10 minutes, the mixed solution was transferred to a Teflon-lined stainless-steel autoclave and reaction at 180 °C for 3 hours. The precipitates were collected by centrifugation and washed with DI water for three times. Subsequently, the Ru-O_x precursor was collected by freeze-drying. Finally, the Ru-O_x-300 was obtained by a thermal treatment under high purity argon (Ar) for 2 hours at 300 °C, with the heating rate of 5 °C min^{-1}.

Materials Characterization

Transmission electron microscopy (TEM), high-angle annular dark-field scanning TEM (HAADF-STEM), and energy-dispersive X-ray spectroscopy (EDS) analyses were performed at 200 kV on a JEOL JEM-2100 F microscope and a FEI Talos microscope at Wuhan University of Technology. Scanning electron microscopy (SEM) images were investigated by HITACHI S-4800 electron microscope. X-ray diffraction (XRD) patterns were measured by Bruker D8 Advance X-ray diffractometer (operating condition: 40 kV, 40 mA) with Cu-Kα radiation (λ = 0.15406 nm). X-ray photoelectron spectroscopy (XPS) measurements were carried out with an ULVAC-PHI PHI Quantera II system, using a monochromated Al-Kα X-ray source, and all spectra were calibrated to a C 1s peak position of 284.8 eV. Fourier transform infrared (FT-IR) spectra were obtained on a Nicolet Avatar 360 FT-IR infrared spectrometer with a Bruker VerTex 80v spectrometer. Raman spectra were conducted on a Renishaw InVia Raman spectrometer under visible excitation at 532 nm. The N_2 adsorption/desorption isotherms of samples were tested at 77 K (TriStar TM II 3020) after outgassing at 120 °C for 12 h. Thermogravimetric and differential scanning calorimetry analysis (TG-DSC) were measured by NETZSCH STA 449 F3 thermogravimetric analyzer (heating rate: 10 °C min^{-1}, atmosphere: Ar). The Ru and B content of the samples was measured by inductively-coupled plasma-atomic emission spectroscopy (ICP-AES, LEEMAN LABS Prodigy7). The water contact angle (CA) of samples were measured by using the sessile-drop method at ambient temperature by an optical contact angle meter (Dataphysics OCA 35). Powdered samples were coated uniformly on a hydrophobic substrate.

Electrochemical Characterization

HER and OER tests.

A three-electrode system was used to perform the electrochemical measurements with an Autolab PGSTAT30 working station from Metrohm. A glassy-carbon rotating disk electrode (RDE) with geometric area of 0.196 cm^2 (diameter: 5 mm) was used as the working electrode. A reversible hydrogen electrode was used as the reference electrode in HER and OER activity tests. An Ag/AgCl electrode

filling with saturated solution of potassium chloride (KCl) was used as reference electrode in HER and OER stability tests, the measured potentials were calibrated to the reversible hydrogen electrode (RHE), with the equation: $E_{vs.RHE} = E_{vs.Ag/AgCl} + 0.197\ V + 0.0592\ V \times pH$. The electrolytes: alkaline seawater (1.0 mol L^{-1} KOH + 3.5% wt. NaCl, pH = 13.8), 0.5 mol L^{-1} H_2SO_4 (pH = 0.1) and 1.0 mol L^{-1} KOH (pH =13.8) were freshly prepared before electrochemical tests.

For the catalyst inks, 5.0 mg of the catalyst powder was dispersed in a mixture solution of isopropyl alcohol (950 μL) and 5% Nafion (50 μL), followed by ultrasonication in an ice-bath for 30 min. 10 μL of the uniformly dispersed catalyst ink was cast onto the RDE; the average mass loading was 0.255 mg cm^{-2}. The cyclic voltammetry (CV) measurements were performed at the scan rate of 100 mV s^{-1} for 20 cycles, and the linear sweep voltammetry (LSV) measurements were performed at the scan rate of 5 mV s^{-1}. The stability measurements were conducted by chrono-potentiometric measurements and applying constant current of -10 mA cm^{-2} (HER) or 10 mA cm^{-2} (OER). All the measurements were under N_2 flow using the glassy carbon RDE at a rotation rate of 1600 rpm. The iR compensation was applied. The electrochemical impedance spectroscopy (EIS) tests were performed at the overpotential of 10 mV over the frequency range of 100 kHz to 0.005 Hz and a small sine-wave distortion (AC signal) of 10 mV amplitude. Electrochemical double layer capacitor (C_{dl}) was derived from double-layer charging curves using CV sweep with scan rate from 20 to 100 mV s^{-1}.

KSCN poisoning experiment was carried out in a three-electrode system by adding different volume of KSCN + alkaline seawater electrolyte in the alkaline seawater electrolyte. In the beginning, the volume of alkaline seawater electrolyte is 35 mL (the concentration of KSCN is 0 mmol L^{-1}), after 400 s, 5 mL of KSCN (2 mmol L^{-1}) + alkaline seawater electrolyte is added in the reaction vessel (the final concentration of KSCN is 0.25 mmol L^{-1}), and after another 400 s, 10 mL of KSCN (1.5 mmol L^{-1}) + alkaline seawater electrolyte is added in the reaction vessel (the final concentration of KSCN is 0.5 mmol L^{-1}) to detect the current density-time curves.

HER and OER performance measurements of Ru-BO_x-OH-300 with different concentrations of BO_3^{3-} in alkaline seawater were measured with a three-electrode system as the previous tests. The pH of electrolyte with different concentrations of BO_3^{3-} in alkaline seawater were controlled to be 13.8.

CO stripping was performed by holding the electrode potential at 0.1 V (vs. RHE) for 10 min in a CO-saturated alkaline seawater electrolyte to adsorb CO on the metal surface, then, removing residual CO in the electrolyte by N_2 purging for 15 min. The CO stripping voltammetry was carried out via LSV in a potential region from 0.2 to 0.9 V (vs. RHE) with scan rate of 5 mV s^{-1}.

Electrochemical measurements for overall water splitting.

The two-electrode cell was performed to make up the full electrolyzer configuration. The titanium (Ti) felt was chosen as the cathode carrier and anode carrier in acidic media and Ni Foam (NF) was used in alkaline electrolyte. The catalyst ink was loaded uniformly on the area of 1.0 × 1.0 cm, the average mass loading is 1.0 mg cm^{-2}. After CV measurements at the scan rate of 100 mV s^{-1} for 20 cycles, the LSV measurements were performed at the scan rate of 5 mV s^{-1} to investigate the overall water splitting performance. The stability measurements were conducted by chrono-potentiometric measurements and applying constant current of 10, 50 and 100 mA cm^{-2}. The solar-driven electrocatalytic water splitting device was performed in an assembled two-electrode H-type electrolytic cell; the electrocatalytic reaction was driven by a commercial silicon solar cell with simulated solar irradiation; the H_2 and O_2 gases were collected by the drainage method with 50 mL measuring cylinder and the starting volume was set to 10 mL. The Faraday efficiency of O_2 was measured with the same method and the OER was occurred in a sealed reactor. The iR compensation was not applied in overall water splitting measurements.

Anion-exchange membrane water electrolyzers (AEMWE) measurements

Anion-exchange membrane water electrolyzers (AEMWE) with serpentine flow channel (effective area: 2.0 × 2.0 cm^2) were used to test practical seawater electrolysis applications of Ru-BO_x-OH-300, commercial Pt/C and RuO_2 electrocatalysts, the electrolyte is 1.0 M KOH + seawater (the seawater is taken from Zhuhai). The Ru-BO_x-OH-300 electrocatalyst ink was sprayed onto Ni foam using an air spray gun and used as cathode and anode plate. The anion exchange membrane (AEM, X37-50 Grade T, Dioxide Materials) was selected as exchange membrane. Subsequently, cathode and anode were sandwiched with an anion exchange membrane and pressed to prepare the MEA. The loading mass of catalyst was approximately 2.5 mg cm^{-2}. The Pt/C and RuO_2 electrodes were prepared by the same method. The AEMWE test was operated at 25 °C with a peristaltic pump pumping 1.0 M KOH + seawater at a flow rate of 15

mL·min^{-1}. The cell performance was obtained from LSV method in a potential region from 1.2 to 2.2 V with scan rate of 5 mV s^{-1}, the iR compensation was not applied. The Long-term stability tests were conducted at the current density of 500 and 1000 mA·cm^{-2}.

Estimation of the Ru dissolution degree.

The chronopotentiometric measurement of Ru-BO_x-OH-300 and Ru-O_x-300 (mass loading of 1.0 mg cm^{-2}) for 20 h at a constant current density of 10 mA cm^{-2} for HER and OER were conducted. The catalysts were loaded on the carbon cloth (CC), the loading area is 1.0 × 1.0 cm. The Ru concentration (C) in the electrolyte were monitored by ICP-AES (Table S4 and S6), the volume of electrolyte is V = 50 mL. The mass of Ru in Ru-BO_x-OH-300 and Ru-O_x-300 are listed in Table S3 and the loading mass (m) of Ru on CC can be calculated. Then, the dissolution degree (D%) of Ru can be estimated as

$$D\%(Ru) = \frac{C(Ru) \times V}{m(Ru)} \times 100\%$$

Methods for detecting Cl_2.

The Hiden HPR-40 DEMS mass spectra (MS) was applied to detect the anode gas, which was collected at 100 mA cm^{-2}. Helium (He) is the carrier gas. If the chlorine (Cl_2) was present in anode gas, signals with the mass of $^{35}Cl_2$ (71) and its isotopes would appear.

Methods for detecting ClO^-.

The chlorine (Cl_2) solubility in water is very high (3.26 g L^{-1} at 25 °C) and it forms hypochlorite (ClO^-) and chloridion (Cl^-) in alkaline solution:

$Cl_2 + 2OH^- \leftrightarrow Cl^- + ClO^- + H_2O$ (1)

The o-tolidine indicator test was conducted to detect if ClO^- formed during at the anode during overall seawater splitting. The o-tolidine indicator was prepared by the following method: 10 mg of o-tolidine was dissolved in 1.5 mL concentrated hydrochloric acid and the solution diluted to 10 mL. After electrocatalytic tests, 400 μL of electrolyte (the total volume is 50 mL) was used for detection. The taken electrolyte was mixed with 400 μL of 0.5 M H_2SO_4 and then 1200 μL of the o-tolidine indicator was added into the mixed solution. If the ClO^- is formed, the color of mixed solution would change from colorless to yellow. Furthermore, the UV-vis spectrum can identify the products and there would an obvious absorption peak around 437 nm if the ClO^- is exist. The oxidation reaction of ClO^- and o-tolidine is listed as follows:[2]

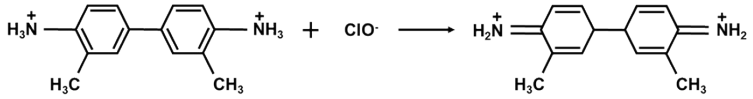

DFT calculations

The density functional theory (DFT) calculations were performed by using the Vienna ab-initio simulation package (VASP).[3] The electron exchange-correlation potential was conducted by Perdew-Burke-Ernzerhof (PBE) functional of generalized gradient approximation (GGA).[4] Also, Perdew-Burke-Ernzerhof (PBE) form generalized gradient approximation (GGA) was used for the exchange-correlation potential. The energy cut‐off for the plane‐wave basis was set to 520 eV. The Brillouin zone in reciprocal space was sampled using the Monkhorst‐Pack scheme with 2 × 2 × 1 k‐point grids for geometry optimization. The dispersion correction was realized by DFT + D3 method.[5] All structures were fully relaxed until the forces were smaller than 0.02 eV Å^{-1}, and the convergence threshold in electronic relaxation was set to 10^{-5} eV using the conjugate gradient algorithm. A vacuum space of 15 Å is applied to each slab.

The reaction Gibbs free energy changes (ΔG) for each elementary steps were based on the computational hydrogen electrode model, which can be calculated by the following equation;

ΔG= ΔE+ ΔZPE-TΔS

where ΔE is obtained directly from DFT calculations, ΔZPE is the change of zero-point energies (ZPE), T is the temperature of 298.15 K, and ΔS is the change in entropy of products and reactants. For the transition states search, the minimum energy pathway for H_2 formation was determined by using a climbing image nudged elastic band method (CINEB).[6]

In addition, the energy of Cl^- is hardly obtained through DFT calculation. In order to calculate the Gibbs free-energy of Cl^- adsorbed on catalysts, we use the follow method.

$* + Cl^- \rightarrow Cl* + e^-$ (2)

$\Delta G1 = G(Cl*) + G(e^-) – G(*) – G(Cl^-)$

$* + H^+ + Cl^- \rightarrow Cl* + (H^+ + e^-)$ (3)

$\Delta G2 = G(Cl*) + [G(H^+) + G(e^-)] – G(*) – G(H^+) - G(Cl^-)$

$* + HCl\ (g) \rightarrow Cl* + (H^+ + e^-)$ (4)

$\Delta G3 = G(Cl*) + [G(H^+) + G(e^-)] – G(*) – G(HCl)$

$HCl\ (g) \rightarrow H^+ + Cl^-\ (aq)$ (5)

$\Delta G4 = G(H^+) + G(Cl^-) – G(HCl)$

$\Delta G4$ can be found in the CRC HANDBOOK of CHEMISTRT and PHYSICS.[7]

Hence, $\Delta G1$ can be obtained by:

$\Delta G1 = \Delta G3 - \Delta G4$

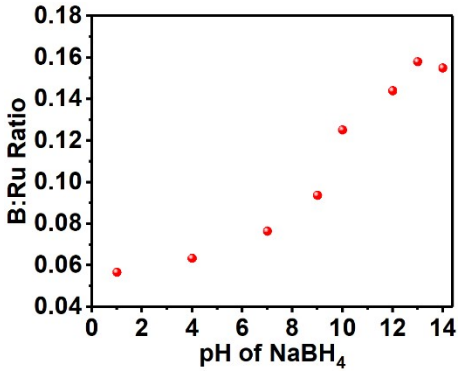

Figure S1. B:Ru atomic ratio of Ru-BO_x-OH precursor related to the pH of $NaBH_4$ solution detected by ICP-AES analysis.

The reduction of Ru ions with $NaBH_4$ is very sensitive to the pH of reacting solution. The metallic Ru is more likely to produce in acidic solution and the ruthenium boride is easier to form in alkaline solution.[8-9] From the ICP-AES analysis (Figure S1), the B:Ru atomic ratio is increased with the pH of $NaBH_4$ solution addition, while the B:Ru atomic ratio of Ru-BO_x-OH precursor didn't further increase when the pH of $NaBH_4$ solution is larger than 13. Therefore, the pH value of $NaBH_4$ solution is chosen to be 13 for preparing the Ru-BO_x-OH precursor.

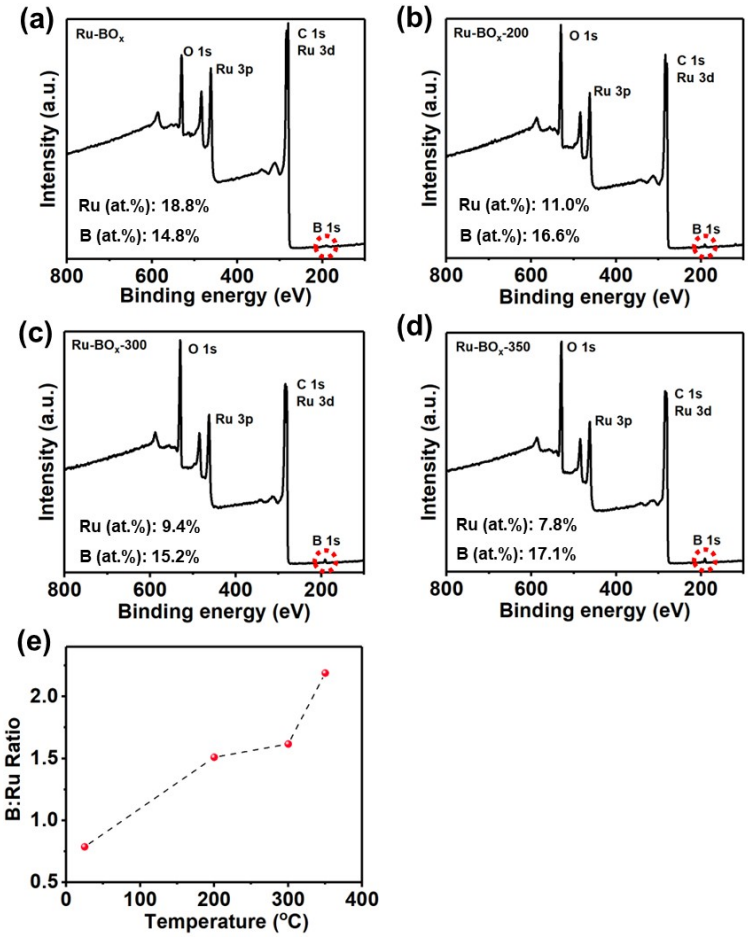

Figure S2. Surface atomic content of ruthenium and boron for (a) Ru-BO_x-OH, (b) Ru-BO_x-OH-200, (c) Ru-BO_x-OH-300, (d) Ru-BO_x-OH-350 and (e) B:Ru atomic ratio related to the annealing temperature from XPS survey results.

Table S1. The ICP-AES content of Ru and B of Ru-BO_x-OH, Ru-BO_x-OH-200, Ru-BO_x-OH-300 and Ru-BO_x-OH-350.

	Ru content (at.%)	B content (at.%)
Ru-BO_x-OH	84.2	15.8
Ru-BO_x-OH-200	83.9	16.1
Ru-BO_x-OH-300	84.5	15.5
Ru-BO_x-OH-350	85.1	14.9

From the ICP-AES analysis in Table S1, the total B:Ru ratio of Ru-BO_x-OH-T has remained relatively unchanged after thermal treatment. However, from XPS results (Figure S2), the B:Ru ratio shows a significant increase with the annealing temperature rising, which indicates the surface borate species increased after the calcination.

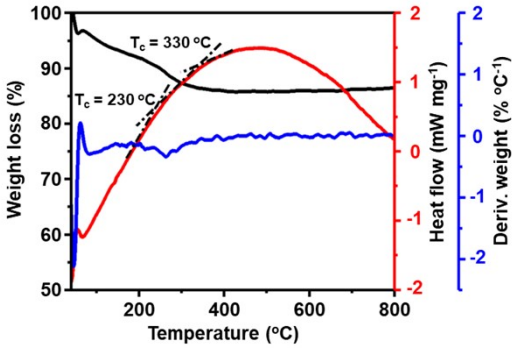

Figure S3. TG-DSC analysis of as-prepared Ru-BO_x-OH in argon.

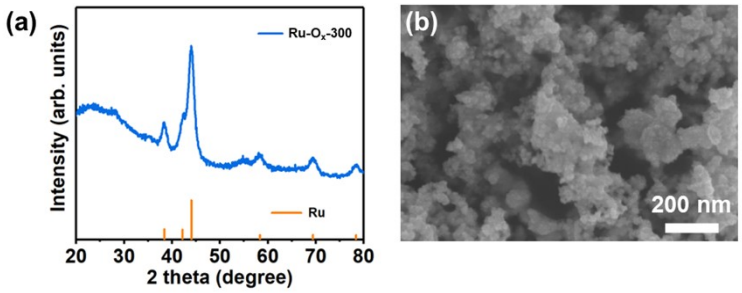

Figure S4. (a) XRD pattern and (b) SEM image of Ru-O_x-300.

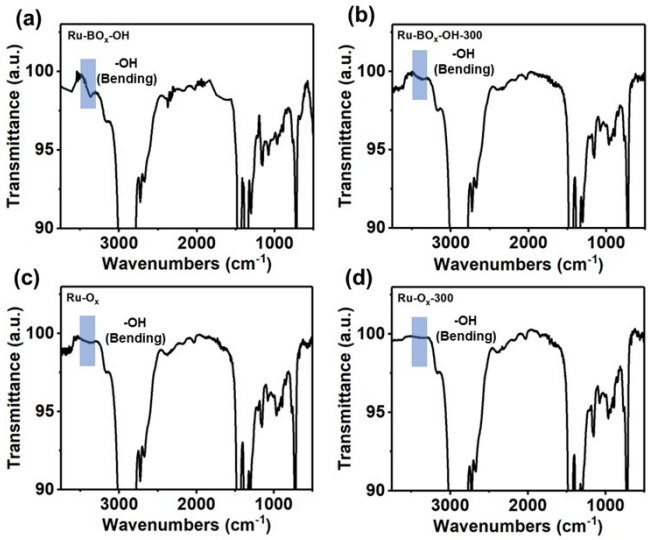

Figure S5. FT-IR spectra of the (a) Ru-BO_x-OH, (b) Ru-BO_x-OH-300, (c) Ru-O_x and (d) Ru-O_x-300 samples, respectively.

The samples were dehydrated with vacuum drying in 150 °C for 24 hours and then recorded in Nujol to avoid the interference of adsorbed H_2O. The main absorption peaks are attributed to Nujol. The absorption peaks at 3500–3600 cm^{-1} are considered to the H-bonding stretching vibrations of the OH group present in the samples.[10] After calcination, the OH absorption peak intensity of Ru-BO_x-OH-300 is higher than Ru-O_x-300.

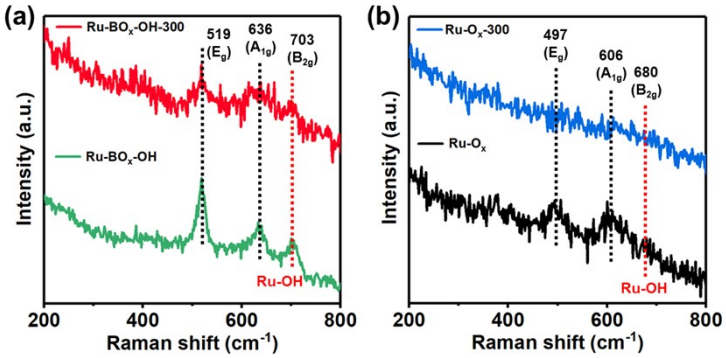

Figure S6. Raman spectra of the (a) Ru-BO_x-OH and Ru-BO_x-OH-300, (b) Ru-O_x and Ru-O_x-300 samples, respectively.

The samples were dehydrated with vacuum drying in 150 °C for 24 hours before testing. The peaks around 525 cm^{-1} and 636 cm^{-1} can be ascribed to the characteristic peaks of RuO_2 (E_g mode at 519 cm^{-1} and A_{1g} mode at 636 cm^{-1}, respectively),[11] a Raman peak of 703 cm^{-1} is ascribed to the interaction of Ru-OH. The Ru-BO_x-OH shows the obvious intensity of RuO_2 and Ru-OH, after 300 °C calcination, their signal intensity can also be detected (Figure S6a). While the signal intensity of RuO_2 and Ru-OH couldn't be detected for Ru-O_x-300 (Figure S6b). The FT-IR and Raman spectra results confirm that Ru-BO_x-OH has rich surface hydroxyl groups and the stable hydroxyl groups are retained after 300 °C calcination.

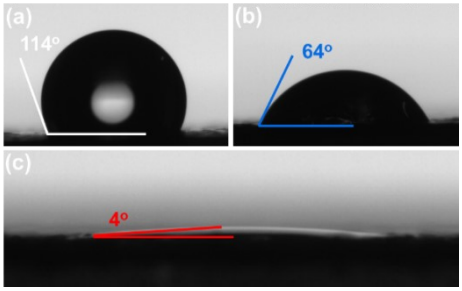

Figure S7. Water contact angle of the (a) pure substrate, (b) Ru-O_x-300 treated substrate and (c) Ru-BO_x-OH-300 treated substrate.

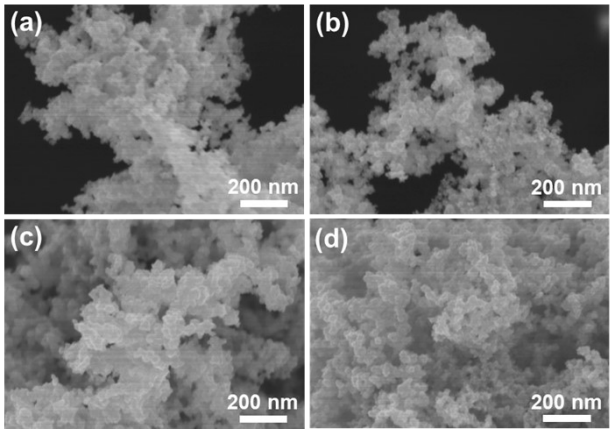

Figure S8. SEM images of (a) Ru-BO_x-OH, (b) Ru-BO_x-OH-200, (c) Ru-BO_x-OH-300 and (d) Ru-BO_x-OH-350.

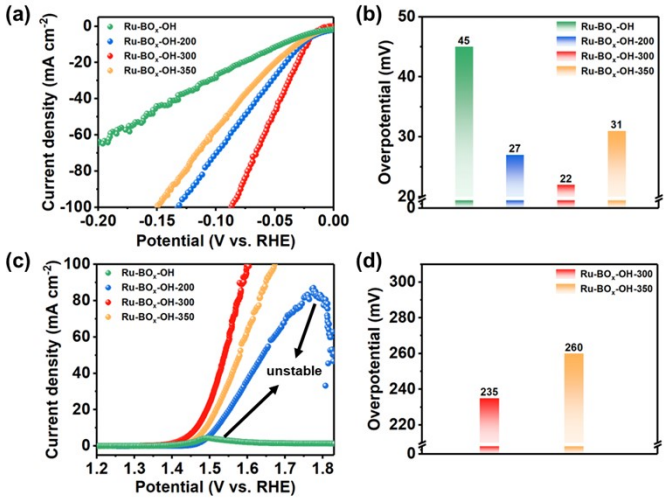

Figure S9. HER and OER performance of Ru-BO_x-OH, Ru-BO_x-OH-200, Ru-BO_x-OH-300 and Ru-BO_x-OH-350 in alkaline seawater. (a) Polarization curves for HER; (b) Comparison of HER overpotential @10 mA cm^{-2}; (c) Polarization curves for OER; (d) Comparison of OER overpotential @10 mA cm^{-2}.

The HER and OER activities show an obvious dependence on the annealing temperatures (Figure S9). The samples calcined between 200 °C to 350 °C present enhanced HER catalytic performance over the Ru-BO_x-OH precursor, while the samples annealed below 200 °C are unstable for OER and Ru-BO_x-OH-300 exhibits the highest activity for both HER and OER. As a result, Ru-BO_x-OH-300 was chosen for further detailed studies.

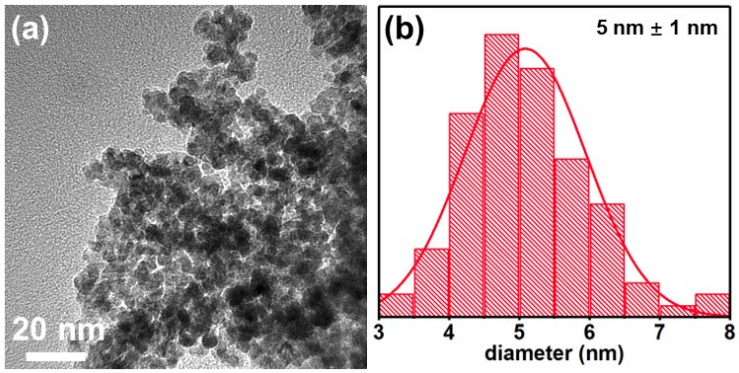

Figure S10. (a) TEM image of Ru-BO_x-OH-300; (b) Histogram of the diameters of nanoparticles.

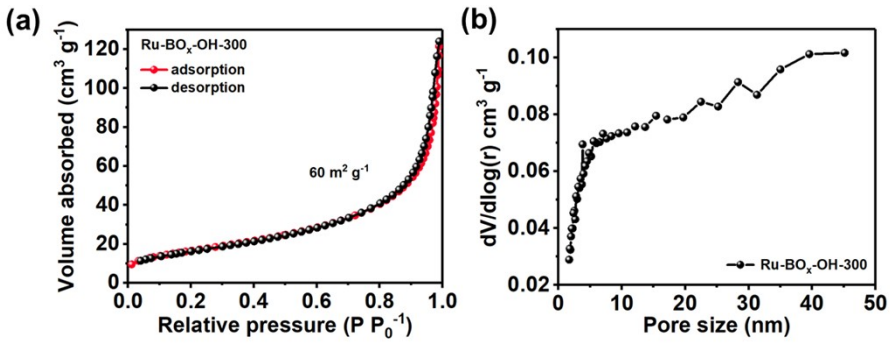

Figure S11. (a) The N_2 adsorption-desorption isotherms and (b) corresponding pore size distribution of Ru-BO_x-OH-300.

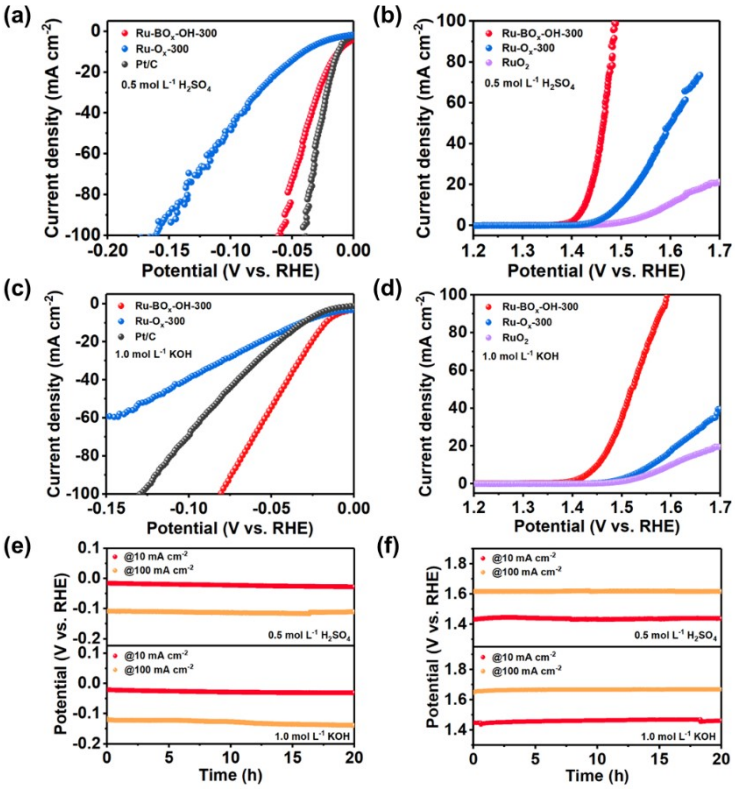

Figure S12. HER and OER performance of Ru-BO$_x$-OH-300, Ru-O$_x$-300, Pt/C and RuO$_2$. (a) Polarization curves for HER in 0.5 mol L^{-1} H$_2$SO$_4$; (b) Polarization curves for OER in 0.5 mol L^{-1} H$_2$SO$_4$; (c) Polarization curves for HER in 1.0 mol L^{-1} KOH; (d) Polarization curves for OER in 1.0 mol L^{-1} KOH. Chronoamperometric test of Ru-BO$_x$-OH-300 at the current density of 10 and 100 mA cm^{-2} for (e) HER and (f) OER in 0.5 mol L^{-1} H$_2$SO$_4$ and 1.0 mol L^{-1} KOH.

Ru-BO$_x$-OH-300 exhibits low overpotentials at 10 mA cm^{-2} for both HER (13 mV, 0.5 mol L^{-1} H$_2$SO$_4$ and 18 mV, 1.0 mol L^{-1} KOH) and OER (196 mV, 0.5 mol L^{-1} H$_2$SO$_4$ and 223 mV, 1.0 mol L^{-1} KOH), it also exhibits excellent stability in 0.5 mol L^{-1} H$_2$SO$_4$ and 1.0 mol L^{-1} KOH electrolyte for both the HER and OER during 20 hours chronoamperometric tests at 10 and 100 mA cm^{-2}.

Table S2. Comparison of HER performance for Ru-BO_x-OH-300 with other reported Ru-based electrocatalysts in acidic and alkaline media.

catalysts	Electrolytes	η@10 (mV @mA cm^{-2})	Ref.
Ru-BO_x-OH-300	**0.5 mol L^{-1} H_2SO_4**	**13**	**This work**
	1.0 mol L^{-1} KOH	**18**	
	1.0 mol L^{-1} KOH + 3.5% wt. NaCl	**22**	
Ru_{SA}@NiFe PPc	0.5 mol L^{-1} H_2SO_4	40	*Energy Environ. Sci.*, 2024, **17**, 1540-1548
	1.0 mol L^{-1} KOH	12	
Ru-VO_2	0.5 mol L^{-1} H_2SO_4	46	*Adv. Mater.*, 2024, **36**, 2310690
	1.0 mol L^{-1} KOH	36	
Mo_2C-Ru/C	0.5 mol L^{-1} H_2SO_4	64	*Adv. Funct. Mater.*, 2024, **34**, 2301925
	1.0 mol L^{-1} KOH	22	
$RuSe_{1.5}$ NPs	0.5 mol L^{-1} H_2SO_4	24	*ACS Catal.,* 2024, **14**, 1914–1921
	1.0 mol L^{-1} KOH	12	
GQDs@ Ru, Mo-Cu_2O/CF	0.5 mol L^{-1} H_2SO_4	39	*Appl. Catal. B-Environ. Energy*, 2024, **344**, 123617
	1.0 mol L^{-1} KOH	30	
Ru@Ir core–shell NSs	0.5 mol L^{-1} H_2SO_4	23	*Appl. Surf. Sci.*, 2024, **651**, 159222
	1.0 mol L^{-1} KOH	29	
Pd_2RuO_x-0.5 h	0.5 mol L^{-1} H_2SO_4	12	*Adv. Mater.*, 2023, **35**, 2208860
	1.0 mol L^{-1} KOH	14	
Ru@1T-MoS_2-MXene	0.5 mol L^{-1} H_2SO_4	44	*Adv. Funct. Mater.*, 2023, **33**, 2212514
	1.0 mol L^{-1} KOH	42	
Mo_2C-Ru/C	0.5 mol L^{-1} H_2SO_4	64	*Adv. Funct. Mater.*, 2023, **34**, 2301925
	1.0 mol L^{-1} KOH	22	
Ru/B-CoP	0.5 mol L^{-1} H_2SO_4	39	*Chem. Eng. J.,* 2023, **452**, 139175
	1.0 mol L^{-1} KOH	52	
Ru/Co–N–C	0.5 mol L^{-1} H_2SO_4	13	*Adv. Mater.*, 2022, **34**, 2110103
	1.0 mol L^{-1} KOH	23	
PtRu/mCNTs	0.5 mol L^{-1} H_2SO_4	15	*Energy Environ. Sci.*, 2022, **15**, 102–108
	1.0 mol L^{-1} KOH	28	
Ru-$Cu(OH)_x$/CF	0.5 mol L^{-1} H_2SO_4	50	*J. Colloid Interf. Sci.,* 2022, **628**, 1061-1069
	1.0 mol L^{-1} KOH	45	
Ru-Ru_2P-4	0.5 mol L^{-1} H_2SO_4	18	*InfoMat*., 2022, **4**, e12287
	1.0 mol L^{-1} KOH	58	
Co_5Ru_1@NCNT/PF	0.5 mol L^{-1} H_2SO_4	45	*Adv. Sci.*, 2022, **9**, 2200010
	1.0 mol L^{-1} KOH	28	

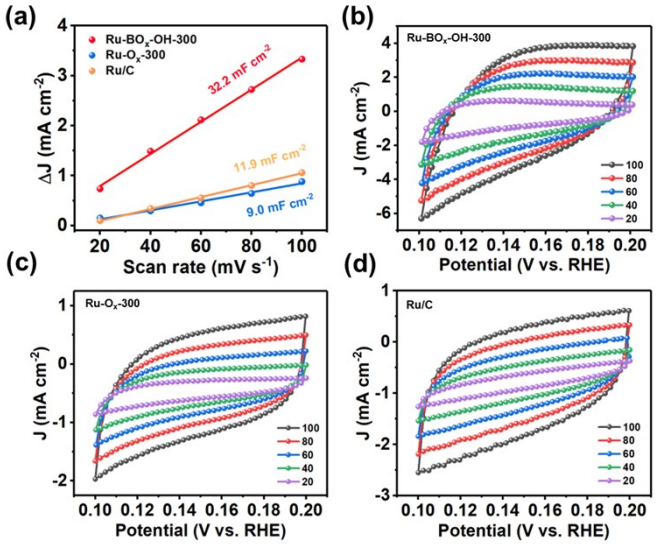

Figure S13. (a) C_{dl} of Ru-BO$_x$-OH-300, Ru-O$_x$-300 and Ru/C by linear fitting of scan rate dependent capacitance currents at 0.15 V (vs. RHE). C_{dl} measurements of (b) Ru-BO$_x$-OH-300, (c) Ru-O$_x$-300 and (d) Ru/C between 0.1 to 0.2 V (vs. RHE) in alkaline seawater.

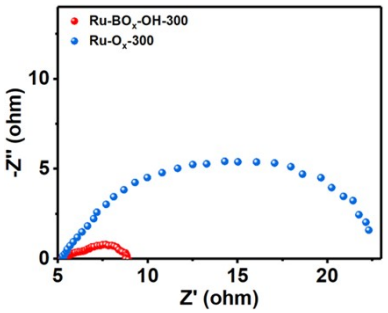

Figure S14. Nyquist plots of Ru-BO$_x$-OH-300 and Ru-O$_x$-300 at -0.03 V (vs. RHE).

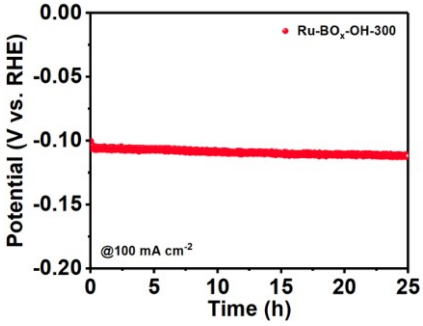

Figure S15. HER chronoamperometric test at the current density of 100 mA cm^{-2} for Ru-BO$_x$-OH-300 in alkaline seawater.

Table S3. ICP analysis for Ru-BO$_x$-OH-300 and Ru-O$_x$-300.

Sample	Sample amount (mg)	Ru (mg)	B (mg)
Ru-BO$_x$-OH-300	5.0	4.01	0.08
Ru-O$_x$-300	5.0	4.11	/

Table S4. ICP analysis of the Ru concentration in electrolyte for Ru-BO_x-OH-300 and Ru-O_x-300 during 20 hours of HER chronoamperometric test at 10 mA cm^{-2}.

	Ru-BO_x-OH-300 (mg L^{-1})	Ru-O_x-300 (mg L^{-1})
2 hours	0.15	0.18
4 hours	0.27	0.31
6 hours	0.34	0.40
8 hours	0.37	0.49
10 hours	0.39	0.51
12 hours	0.40	0.54
14 hours	0.41	0.56
16 hours	0.42	0.57
18 hours	0.43	0.57
20 hours	0.43	0.58

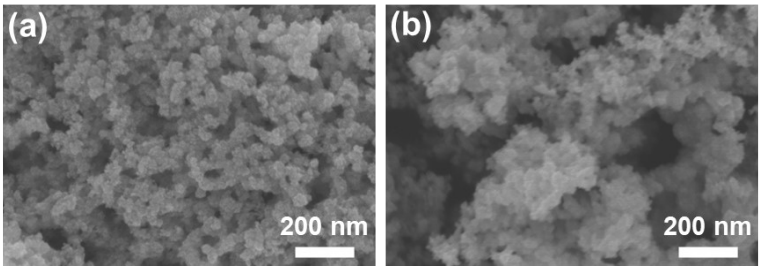

Figure S16. SEM images of (a) Ru-BO_x-OH-300 and (b) Ru-O_x-300 after HER stability tests of 20 hours. Compare to Figure S8 for SEM images before the stability test.

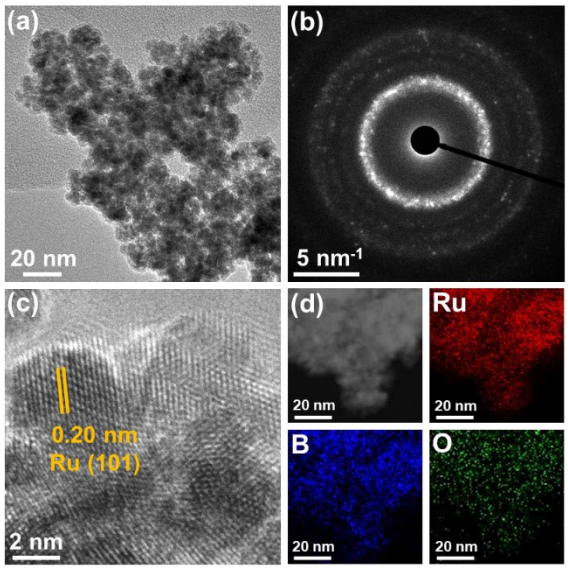

Figure S17. TEM images of Ru-BO_x-OH-300 after HER stability tests of 20 hours. (a) TEM image of Ru-BO_x-OH-300. (b) Corresponding SAED pattern of Figure S17a. (c) HRTEM image of Ru-BO_x-OH-300. (d) HAADF-STEM image of Ru-BO_x-OH-300 and EDX mapping images of Ru, B and O. Compare to Figure 2 for TEM images before the stability test.

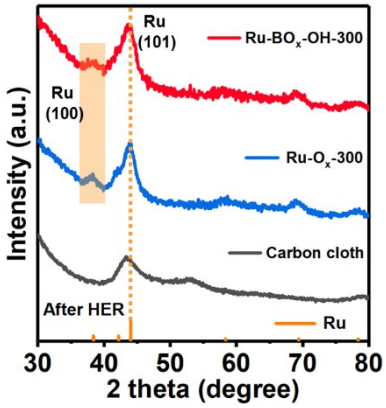

Figure S18. XRD patterns of bare carbon cloth, Ru-BO$_x$-OH-300 and Ru-O$_x$-300 electrodes after HER stability tests of 20 hours. Compare to Figure 1b before the stability test, the catalysts were loaded on carbon cloth as electrodes and the mass loading is 1.0 mg cm^{-2}.

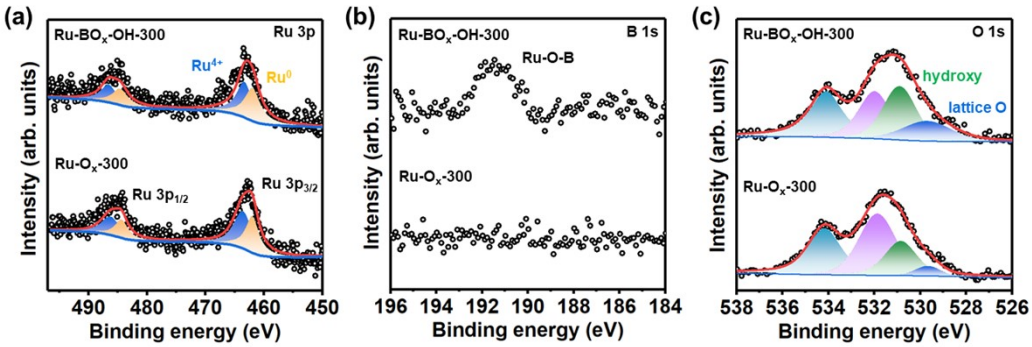

Figure S19. XPS spectra of Ru-BO$_x$-OH-300 and Ru-O$_x$-300 electrodes after HER stability tests of 20 hours. Compare to Figure 1 for XPS spectra before the stability test, the catalysts were loaded on carbon cloth as electrodes and the mass loading is 1.0 mg cm^{-2}.

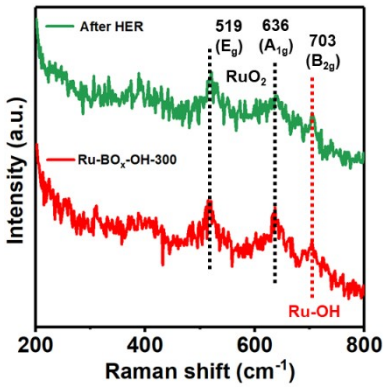

Figure S20. Raman spectra of Ru-BO$_x$-OH-300 and Ru-BO$_x$-OH-300 after HER stability tests of 20 hours.

Table S5. Comparison of OER performance for Ru-BO_x-OH-300 with other reported Ru-based electrocatalysts in acidic and alkaline media.

catalysts	Electrolytes	η@10 (mV @mA cm^{-2})	Ref.
Ru-BO_x-OH-300	**0.5 mol L^{-1} H_2SO_4**	**196**	**This work**
	1.0 mol L^{-1} KOH	**223**	
	1.0 mol L^{-1} KOH + 3.5% wt. NaCl	**235**	
Ru-VO_2	0.5 mol L^{-1} H_2SO_4	228	*Adv. Mater.*, 2024, **36**, 2310690
	1.0 mol L^{-1} KOH	227	
Ru@Ir core–shell NSs	0.5 mol L^{-1} H_2SO_4	246	*Appl. Surf. Sci.*, 2024, **651**, 159222
	1.0 mol L^{-1} KOH	233	
$Ru_xCr_{1-x}O_y$_20	0.5 mol L^{-1} H_2SO_4	210	*J. Mater. Chem. A*, 2023, **11**, 26626-26635
	1.0 mol L^{-1} KOH	240	
Ru/RuO_{2NB}/C	0.5 mol L^{-1} H_2SO_4	276	*Chem. Eng. J.,* 2023, **468**, 143761
	1.0 mol L^{-1} KOH	290	
$RuIrO_x$@NHC	0.5 mol L^{-1} H_2SO_4	250	*Small*, 2023, 2308841
	1.0 mol L^{-1} KOH	258	
FRNO/CC	0.5 mol L^{-1} H_2SO_4	200	*Adv. Energy Mater.*, 2023, **13**, 2300174
	1.0 mol L^{-1} KOH	260	
Ru_2Co_1BO-350	0.5 mol L^{-1} H_2SO_4	211	*Nano Lett.*, 2023, **23**, 1052−1060
	1.0 mol L^{-1} KOH	222	
Ru-O-Mn/CPD	0.5 mol L^{-1} H_2SO_4	196	*Appl. Catal. B: Environ.*, 2023, **328**, 122546
	1.0 mol L^{-1} KOH	194	
Ru/Co–N–C-800 °C	0.5 mol L^{-1} H_2SO_4	232	*Adv.Mater.*, 2022, **34**, 2110103
	1.0 mol L^{-1} KOH	276	
RuO_2-C-300	0.5 mol L^{-1} H_2SO_4	198	*Small*, 2022, **18**, 2203778
	1.0 mol L^{-1} KOH	270	
$Ru_{0.75}Ir_{0.25}$	0.5 mol L^{-1} H_2SO_4	219	*Chem. Eng. J.,* 2022, **450**, 137909
	1.0 mol L^{-1} KOH	210	
Ru@$MoO(S)_3$	0.5 mol L^{-1} H_2SO_4	226	*Nano Energy*, 2022, **100**, 107445
	1.0 mol L^{-1} KOH	265	
$CoRuO_x$@C	0.5 mol L^{-1} H_2SO_4	223	*Appl. Surf. Sci.*, 2022, **606**, 154818
	1.0 mol L^{-1} KOH	240	
$Ni_{cluster}$–Ru NWs	0.5 mol L^{-1} H_2SO_4	205	*Energy Environ. Sci.*, 2021, **14**, 3194-3202
	1.0 mol L^{-1} KOH	194	
a/c-RuO_2	0.5 mol L^{-1} H_2SO_4	220	*Angew. Chem.*, 2021, **133**, 18969–18977
	1.0 mol L^{-1} KOH	235	

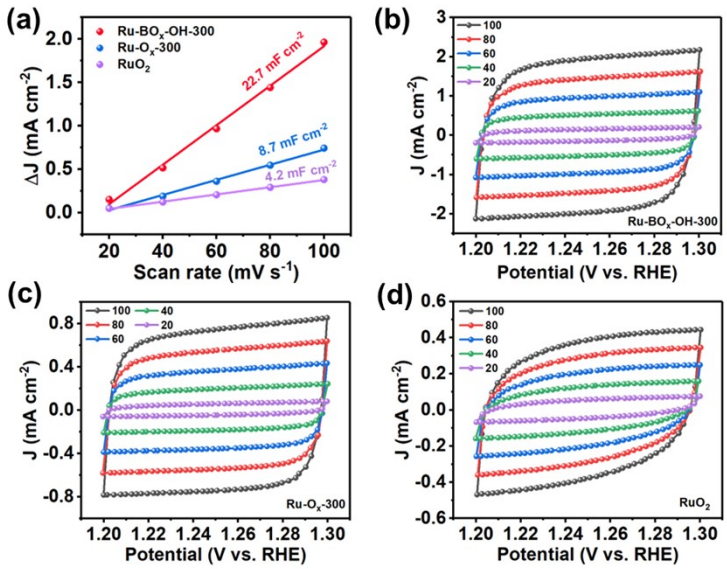

Figure S21. (a) C_{dl} of Ru-BO_x-OH-300, Ru-O_x-300 and RuO_2 by linear fitting of scan rate dependent capacitance currents at 1.25 V (vs. RHE). C_{dl} measurements of (b) Ru-BO_x-OH-300, (c) Ru-O_x-300 and (d) RuO_2 between 1.2 to 1.3 V (vs. RHE) in alkaline seawater.

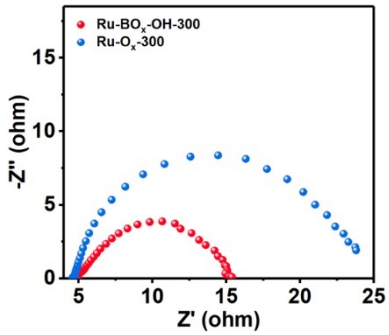

Figure S22. Nyquist plots of Ru-BO_x-OH-300 and Ru-O_x-300 at 1.46 V (vs. RHE).

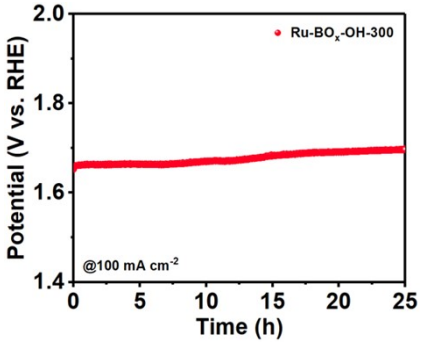

Figure S23. OER chronoamperometric test at the current density of 100 mA cm^{-2} for Ru-BO_x-OH-300 in alkaline seawater.

Table S6. ICP analysis of the Ru concentration in electrolyte for Ru-BO_x-OH-300 and Ru-O_x-300 during 20 hours of OER chronoamperometric test at 10 mA cm^{-2}.

	Ru-BO_x-OH-300 (mg L^{-1})	Ru-O_x-300 (mg L^{-1})
2 hours	0.4	3.0
4 hours	0.5	4.4
6 hours	0.7	5.3
8 hours	0.8	5.9
10 hours	1.0	6.5
12 hours	1.1	6.8
14 hours	1.1	/
16 hours	1.3	/
18 hours	1.3	/
20 hours	1.4	/

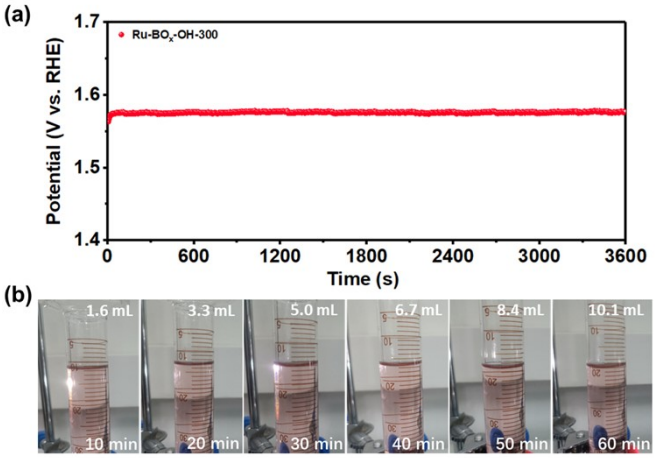

Figure S24. (a) Chronoamperometric test at the current density of 45 mA cm^{-2} for Ru-BO_x-OH-300 electrode. (b) Photographs of collected O_2 at different times. The starting volume was set to 10 mL.

Table S7. The amount of collected H_2 and O_2 gases.[a]

	10 min	20 min	30 min	40 min	50 min	60 min
Collected O_2 (mL)	1.6	3.3	5.0	6.7	8.4	10.1
Theoretical O_2 (mL)	1.7	3.4	5.1	6.9	8.6	10.3

[a] The accuracy of the volume readings was about ±0.2 mL

The Faradaic efficiency of O_2 is calculated by dividing the amount of O_2 gas collected experimentally by the theoretical oxygen production calculated using the volume value. The gases were collected at 25 °C under one atmosphere and the molar volume of gas is 24.5 L mol^{-1}. The current density is 45 mA cm^{-2} (area of electrode: 1 cm^2) during the OER. The Faraday constant is 96485 C mol^{-1}. Theoretical O_2 volume = (0.045 A × t s / 96485 C mol^{-1}) / 4 *24.5 L/mol, where "t" is the tested time. The Faradaic efficiency of O_2 is calculated as 98.1%.

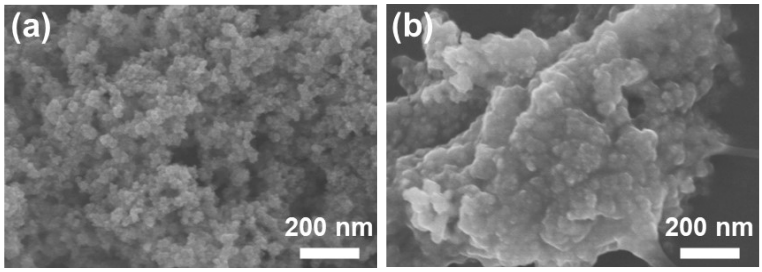

Figure S25. SEM images of (a) Ru-BO_x-OH-300 and (b) Ru-O_x-300 after OER stability tests for 20 hours. Compare to Figure S8 for SEM images before the stability test.

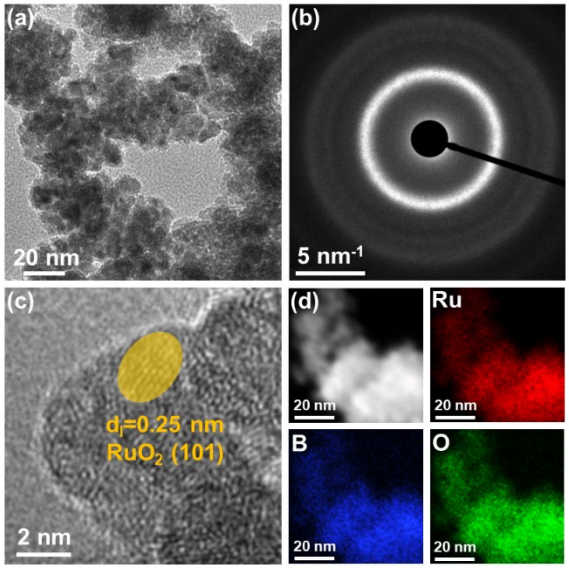

Figure S26. TEM images of Ru-BO_x-OH-300 after OER stability tests of 20 hours. (a) TEM image of Ru-BO_x-OH-300. (b) Corresponding SAED pattern of Figure S26a. (c) HRTEM image of Ru-BO_x-OH-300. (d) HAADF-STEM image of Ru-BO_x-OH-300 and EDX mapping images of Ru, B and O. Compare to Figure 2 for TEM images before the stability test.

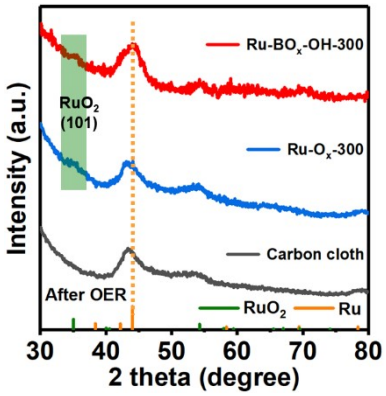

Figure S27. XRD patterns of bare carbon cloth, Ru-BO$_x$-OH-300 and Ru-O$_x$-300 electrodes after OER stability tests for 20 hours. Compare to Figure 1b for PXRD patterns before the stability test. The catalysts were loaded on carbon cloth as electrodes and the mass loading is 1.0 mg cm^{-2}.

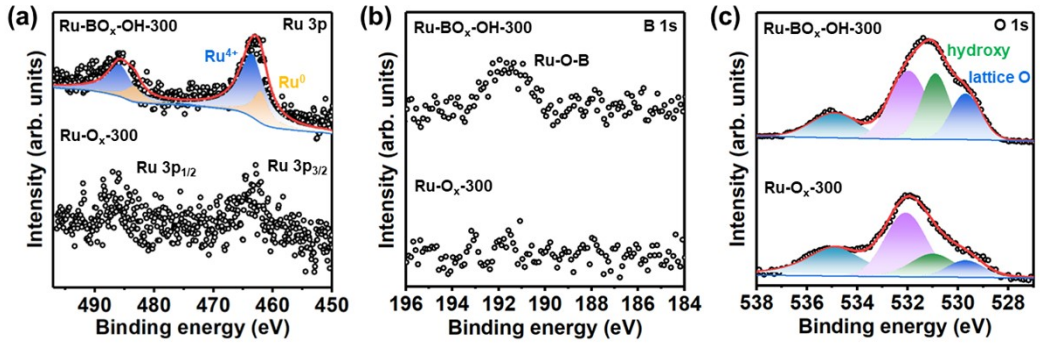

Figure S28. XPS spectra of Ru-BO$_x$-OH-300 and Ru-O$_x$-300 electrodes after OER stability tests of 20 hours. Compare to Figure 1 for XPS spectra before the stability test, the catalysts were loaded on carbon cloth as electrodes and the mass loading is 1.0 mg cm^{-2}.

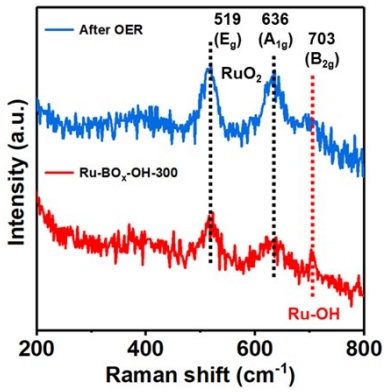

Figure S29. Raman spectra of Ru-BO$_x$-OH-300 and Ru-BO$_x$-OH-300 after OER stability tests of 20 hours.

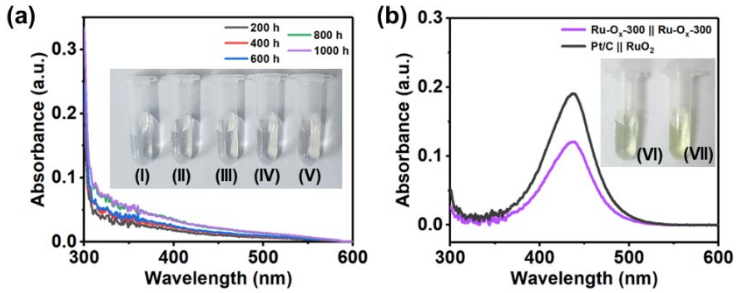

Figure S30. UV-vis spectra of the testing solutions after overall seawater splitting for (a) Ru-BO_x-OH-300 || Ru-BO_x-OH-300 after seawater splitting tests of 1000 hours at 10, 50 and 100 mA cm^{-2} and (b) Ru-O_x-300 || Ru-O_x-300 and Pt/C || RuO_2 after seawater splitting tests at 10 mA cm^{-2}. The inset digital graphs of the corresponding mixed solutions for Ru-BO_x-OH-300 || Ru-BO_x-OH-300 after seawater splitting for (I) 200 hours at 10 mA cm^{-2}, (II) 400 hours at 50 mA cm^{-2}, (III) 600 hours at 50 mA cm^{-2}, (IV) 800 hours at 100 mA cm^{-2} and (V) 1000 hours at 100 mA cm^{-2}. (VI) Ru-O_x-300 || Ru-O_x-300 after seawater splitting test at 10 mA cm^{-2}. (VII) Pt/C || RuO_2 after seawater splitting test at 10 mA cm^{-2}.

O-Tolidine was utilized to detect whether the ClO^- is formed at anode. As is shown in Figure S30a, the color of mixed solutions for Ru-BO_x-OH-300 || Ru-BO_x-OH-300 after seawater splitting tests are colorless and there is no adsorption peak, indicating that no ClO^- is formed during seawater splitting. While the color of mixed solutions for Ru-O_x-300 || Ru-O_x-300 and Pt/C || RuO_2 after seawater splitting tests are both turned into yellow and there are obvious absorption peaks around 437 nm (Figure S30b), conforming the formation of ClO^-.

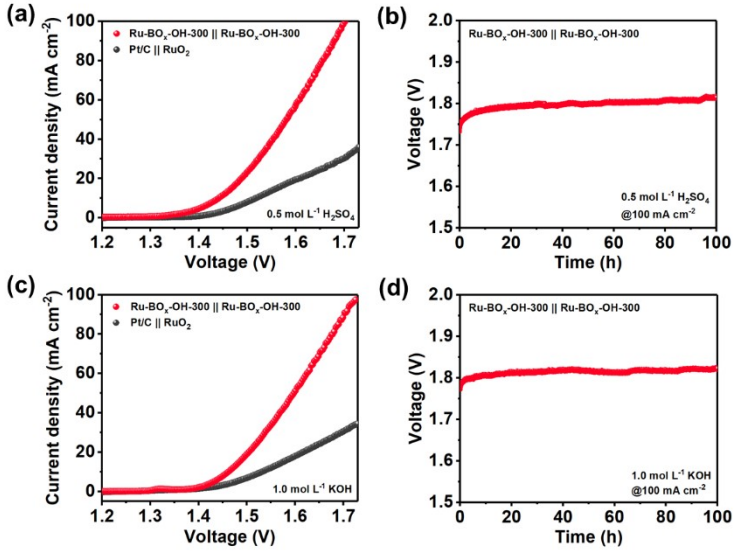

Figure S31. Polarization curves for overall water splitting of Ru-BO_x-OH-300 || Ru-BO_x-OH-300 in (a) 0.5 mol L^{-1} H_2SO_4 and (c) 1.0 mol L^{-1} KOH electrolyte, respectively. Long-term stability of Ru-BO_x-OH-300 || Ru-BO_x-OH-300 for overall water splitting at the current density of 100 mA cm^{-2} in (b) 0.5 mol L^{-1} H_2SO_4 and (d) 1.0 mol L^{-1} KOH solution, respectively.

The Ru-BO_x-OH-300 || Ru-BO_x-OH-300 device shows high activity in overall water splitting in both acidic and alkaline electrolyte with voltages of 1.44 V (0.5 mol L^{-1} H_2SO_4) and 1.46 V (1.0 mol L^{-1} KOH) at 10 mA cm^{-2}. Also, it has a high durability reflected in its operation without obvious decay for at least 100 hours at 100 mA cm^{-2} in 0.5 mol L^{-1} H_2SO_4 and 1.0 mol L^{-1} KOH electrolyte.

Table S8. Comparison of overall water splitting performance for Ru-BO_x-OH-300 with other reported electrocatalysts in different media.

catalysts	Electrolytes	Voltage (V @ 10 mA cm^{-2})	Stability time (h)	Ref.
Ru-BO_x-OH-300	**0.5 mol L^{-1} H_2SO_4** **1.0 mol L^{-1} KOH + 3.5% wt. NaCl** **1.0 mol L^{-1} KOH**	**1.44** **1.47** **1.46**	**1000**	**This work**
Ru-VO_2	0.5 mol L^{-1} H_2SO_4 1.0 mol L^{-1} KOH 1.0 mol L^{-1} PBS	1.515 1.54 1.63	125	*Adv. Mater.,* 2024, **36**, 2310690
Ru/d-NiFe LDH	1.0 mol L^{-1} KOH	1.49	100	*Adv. Energy Mater.*, 2024, 2400059
Ru NCs/P,O-NiFe LDH/NF	1.0 mol L^{-1} KOH 1.0 mol L^{-1} KOH + 0.5 M NaCl	1.466 1.506	44.4	*Adv. Funct. Mater.* 2024, **34**, 2310690
Ru-Co_2P@Ru-N-C	1.0 mol L^{-1} KOH	1.56	22	*Adv. Funct. Mater.*, 2024, 2316709
RuO_2/CeO_2@C	0.5 mol L^{-1} H_2SO_4	1.54	100	*Chem. Eng. J.,* 2024, **479**, 147939
RCO-V_O@CC	1.0 mol L^{-1} KOH	1.49	120	*Small*, 2024, 2309633
Ru/NF	1.0 mol L^{-1} KOH	1.50	24	*Nanoscale,* 2024, **16**, 6662–6668
CPF-Fe/Ni	0.5 mol L^{-1} H_2SO_4 1.0 mol L^{-1} KOH	1.44 1.57	120	*Nat. Commun.*, 2023, **14**, 1792
Ru@V-RuO_2/C HMS	0.5 mol L^{-1} H_2SO_4 1.0 mol L^{-1} KOH	1.467 1.437	25	*Adv. Mater.*, 2023, **35**, 2206351
$Ru_{0.85}Zn_{0.15}O_{2-\delta}$	0.5 mol L^{-1} H_2SO_4 1.0 mol L^{-1} KOH	1.50 1.47	50	*Adv. Energy Mater.*, 2023, **13**, 2300177
$RuIrO_x$@NHC	0.5 mol L^{-1} H_2SO_4 1.0 mol L^{-1} KOH 1.0 mol L^{-1} KOH + seawater	1.53 1.51 1.54	225	*Small*, 2023, 2308841
Ru/Mo_2C	0.5 mol L^{-1} H_2SO_4	1.51	12	*Electrochimica Acta*, 2023, **443**, 141920
RuO_2/C_3N_4	0.5 mol L^{-1} H_2SO_4	1.607	28	*Dalton Trans.*, 2023, **52**, 10515–10521
Ru SAs-MoO_{3-x}/NF	1.0 mol L^{-1} KOH	1.487	180	*Adv. Sci.*, 2023, **10**, 2300342

Ru_2Co_1BO-350	0.5 mol L^{-1} H_2SO_4 1.0 mol L^{-1} KOH + 3.5% wt. NaCl 1.0 M KOH	1.452 1.466 1.463	230	*Nano Lett.*, 2023, **23**, 1052−1060
Ru_1Cu_1 NTs	0.5 mol L^{-1} H_2SO_4 1.0 mol L^{-1} KOH	1.59 1.50	100	*Chem. Eng. J.,* 2023, **456**, 141148
$NiRuO_{2-x}$	1.0 mol L^{-1} KOH	1.6	20	*J. Colloid Interf. Sci.,* 2023, **630**, 940–950
Pt-$Ni(OH)_2$ @NM	1.0 mol L^{-1} KOH	1.491	600	*Appl. Catal. B: Environ.*, 2023, **325**, 122296
ZIF-67@CNT	1.0 mol L^{-1} KOH	1.53	800	*Electrochimica Acta*, 2023, **439**, 141593
IrPdRhMoW/CP	0.5 mol L^{-1} H_2SO_4	1.48	100	*Chinese J. Catal.*, 2023, **45**, 174-183
CoNiRu-NT	1.0 mol L^{-1} KOH	1.47	48	*Adv. Mater.,* 2022, **34**, 2107488
PtIr/IrO_x NWs	1.0 mol L^{-1} KOH	1.52	400	*Small*, 2022, **18**, 2201333
Ni-CoP/Co_2P@NC	1.0 mol L^{-1} KOH	1.59	400	*Chem. Eng. J.*, 2022, **433**, 133523
IrO_2@MnO_2/rGO	1.0 mol L^{-1} KOH 1.0 mol L^{-1} KOH + 1.0 mol L^{-1} NaCl 1.0 mol L^{-1} KOH + seawater	1.60 1.58 1.64	300	*ACS Sustainable Chem. Eng.,* 2022, **10**, 15068-15081
RuO_2-C-300	1.0 mol L^{-1} KOH + seawater 1.0 mol L^{-1} KOH	1.52 1.50	100	*Small*, 2022, **18**, 2203778
RNC-O-75	0.5 mol L^{-1} H_2SO_4	1.56	40	*J. Alloy. Compd.*, 2022, **902**, 163787
RuIrTe NTs	0.5 mol L^{-1} H_2SO_4	1.511	24	*J. Mater. Chem. A*, 2022, **10**, 2021–2026
NiMoRuO	1.0 mol L^{-1} KOH	1.56	30	*Chem. Eng. J.,* 2021, **420**, 127686
Ru-NiCoP/NF	1.0 mol L^{-1} KOH	1.515	50	*Appl. Catal. B: Environ.*, 2020, **279**, 119396

Figure S32. A photo showing a commercial silicon solar cell-driven electrolysis (1 cm^2 electrodes) of alkaline seawater.

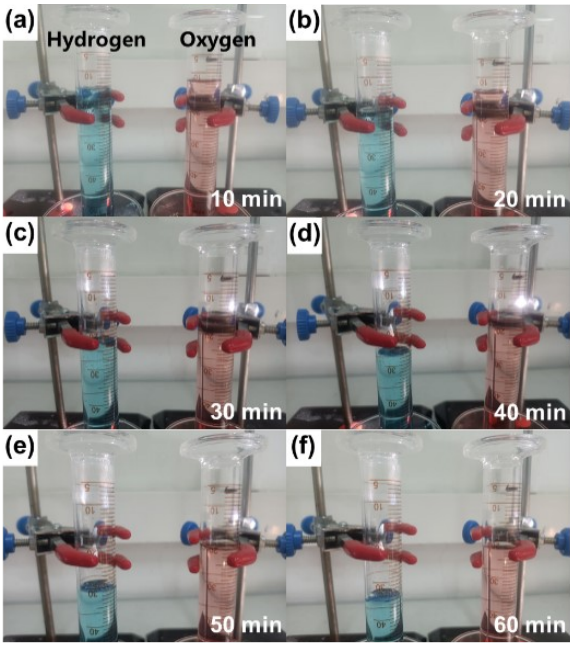

Figure S33. Photographs of collected H_2 and O_2 at different times. The starting volume was set to 10 mL.

Table S9. The amount of collected H_2 and O_2 gases.[b]

	10 min	20 min	30 min	40 min	50 min	60 min
Collected H_2 (mL)	4.0	8.2	12.4	16.6	20.8	25.0
Theoretical H_2 (mL)	4.2	8.4	12.6	16.8	20.9	25.1
Collected O_2 (mL)	2.0	4.0	6.2	8.2	10.2	12.5
Theoretical O_2 (mL)	2.1	4.2	6.3	8.4	10.5	12.6

[b] The accuracy of the volume readings was about ±0.2 mL

The Faradaic efficiency of H_2 is calculated by dividing the amount of H_2 gas collected experimentally by the theoretical hydrogen production calculated using the volume-time slope value in Figure 5f. The gases were collected at 25 °C under one atmosphere and the molar volume of gas is 24.5 L mol^{-1}. The current density is 55 mA cm^{-2} (area of electrode: 1 cm^2) during the overall seawater electrolysis. The Faraday constant is 96485 C mol^{-1}. Theoretical H_2 volume = (0.055 A × t s / 96485 C mol^{-1}) / 2 *24.5 L/mol, where "t" is the tested time. The theoretical values of H_2 and O_2 are calculated in the Table S9. From the dividing of collected gas slope by theoretical gas slope in Figure 5f, the Faradaic efficiency of H_2 and O_2 is calculated as 97.6%.

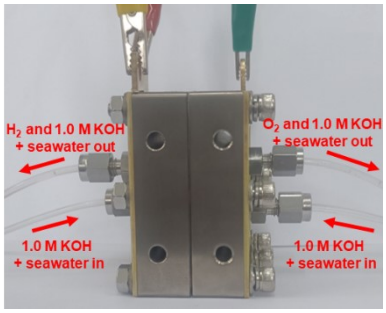

Figure S34. Photograph of the AEM electrolyzer.

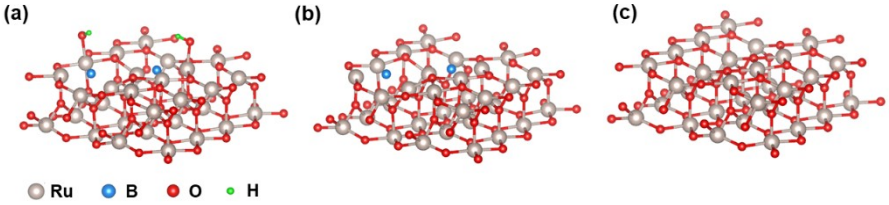

Figure S35. Structure models of optimized structure of (a) RuO_x-BO_x-OH, (b) RuO_x-BO_x and (c) RuO_2.

According to the structure analysis of Ru-BO_x-OH-300 catalysts after OER stability tests (Figure S25-S29), the species of RuO_2 mixed with borate and hydroxyl groups are formed in the Ru-BO_x-OH-300 nanoparticles during OER, which are considered to be reactive sites and the (110) crystal plane of RuO_2 mixed with hydroxyl groups and boron species model is simulated as reactive species of Ru-BO_x-OH-300 catalyst during OER (Figure S35a). The model only with boron species on (110) crystal plane of RuO_2 surface is also established to figure out the effects of hydroxyl groups during seawater splitting process (Figure S35b). The (110) crystal plane of RuO_2 is simulated as reactive species of Ru-O_x-300 catalyst during OER (Figure S35c).

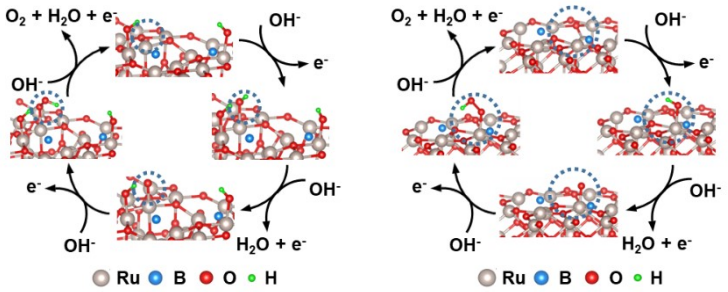

Figure S36. Proposed $4e^-$ mechanism reaction pathway of OER on (a) RuO_x-BO_x-OH and (b) RuO_x-BO_x.

The $4e^-$ mechanism reaction pathway of OER was shown in Figure S36, the reactive sites are regarded as Ru atoms and the reaction equations are as follows:

$Ru + OH^- \rightarrow Ru\text{-}OH + e^-$

$Ru\text{-}OH + OH^- \rightarrow Ru\text{-}O + H_2O + e^-$

$Ru\text{-}O + OH^- \rightarrow Ru\text{-}OOH + e^-$

$Ru\text{-}OOH + OH^- \rightarrow Ru + O_2 + H_2O + e^-$

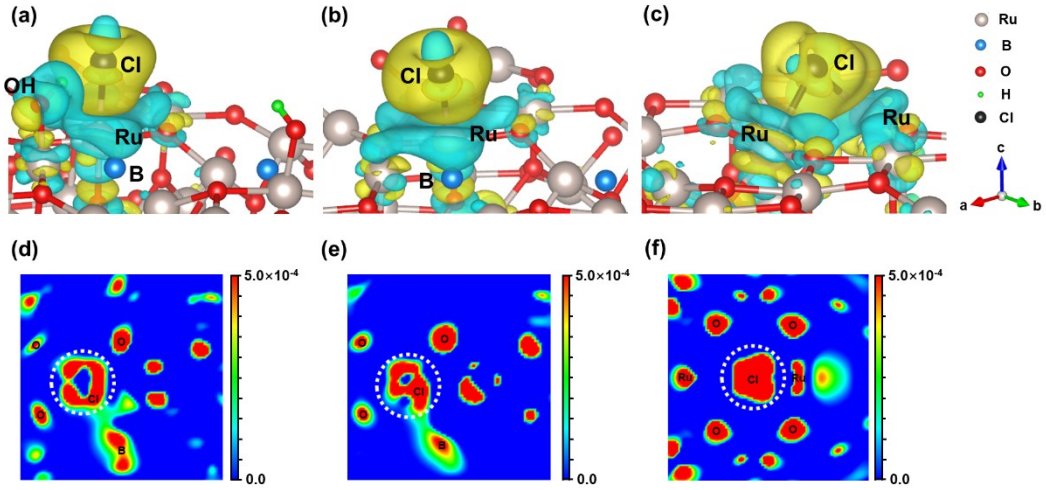

Figure S37. The differential charge density distribution of the adsorption of Cl^- on (a) RuO_x-BO_x-OH, (b) RuO_x-BO_x and (c) RuO_2 models. Charge density distributions in models of (d) RuO_x-BO_x-OH, (e) RuO_x-BO_x and (f) RuO_2 adsorbed a Cl^-.

References

1. H. Z. Yu, Y. Wang, J. Ying, S. M. Wu, Y. Lu, J. Hu, J. S. Hu, L. Shen, Y. X. Xiao, W. Geng, G. G. Chang, C. Janiak, W. H. Li and X. Y. Yang, *ACS Appl. Mater. Interfaces* 2019, **31**, 27641-27647.
2. J. Li, Y. Liu, H. Chen, Z. Zhang, X. Zou, *Adv. Funct. Mater.,* 2021, **31**, 2101820.
3. G. Kresse, J. Hafner, *Phys. Rev. B. Condens. Matter*. 1993, **47**, 558-561
4. J. P. Perdew, K. Burke, M. Ernzerhof, *Phys. Rev. Lett.* 1996, **77**, 3865-3868.
5. S. Grimme, *J. Comput. Chem.* 2006, **27**, 1787-1799.
6. G. Henkelman, B. P. Uberuaga and H. Jónsson, *J. Chem. Phys.* 2000, **113**, 9901.
7. Haynes W M. CRC handbook of chemistry and physics [M]. CRC press, 2016.
8. J. Lu, D. B. Dreisinger, W. C. Cooper, *Hydrometallurgy* 1997, **45**, 305-322.
9. J. Masa, P. Weide, D. Peeters, I. Sinev, W. Xia, Z. Sun, C. Somsen, M. Muhler, W. Schuhmann, *Adv. Energy Mater.* 2016, **6**, 1502313.
10. M.A.R. George, N.X. Truong, M. Savoca and O. Dopfer, *Angew. Chem. Int. Ed.* 2018, **57**, 2919-2923.
11. L. Meng, V. Teixeira, M.P. dos Santos, *Thin Solid Films* 2003, **442**, 93-97.